Experimental Thermal and Fluid Science 98 (2018) 719–730

Contents lists available at ScienceDirect

Experimental Thermal and Fluid Science

journal homepage: www.elsevier.com/locate/etfs

# Flow instability evolution in high pressure ratio centrifugal compressor with vaned diffuser

Xiao He, Xinqian Zheng*

*Department of Automotive Engineering, Turbomachinery Laboratory, State Key Laboratory of Automotive Safety and Energy, Tsinghua University, Beijing 100084, China*

ARTICLE INFO

*Keywords:*
Compressor stability
Centrifugal compressor
Surge
Stall
Rotating instability

ABSTRACT

Compressor stability is an essential issue for developing single-stage high pressure ratio centrifugal compressors. In this paper, a comprehensive stability map of a centrifugal compressor stage with the peak pressure ratio of 6.2 has been illustrated. Fast response pressure transducers are mounted inside the casing or the back-plate wall to measure internal transient behaviors. From Fourier analysis of pressure signals, various instabilities across time and length scales are identified. At low speeds, the impeller inlet rotating instability develops in scale and evolves into the inducer stall, which eventually induces the mild surge and deep surge of the compression system. At middle speeds, the compressor successively experiences stable state, mild surge, rotating instability, and deep surge. The mild surge region coincides with the dip region of the compressor S-shape pressure rise curve, and deep surge occurs when the compressor pressure rise raises to the second peak. At high speeds, mild surge and deep surge abruptly occur without preceding stall or rotating instability. To explain the complex surge behavior, the mechanical analogy between the compression system and the mass-spring-damper system is applied. Both mild surge and deep surge transients are found to belong to the dynamic instability of the mass-spring-damper system, and the exact form of the surge state will be determined by eigenvalues of the system governing equation.

## 1. Introduction

Centrifugal compressors are widely applied in automobile, aviation, oil and gas industries. For reduction of manufacturing cost and engine weight, high pressure ratio centrifugal compressors are especially preferred in the aviation industry [1]. However, due to the rapid drop in stable flow range with increasing pressure ratio [2], the application of high pressure ratio centrifugal compressors is still limited. The key challenge of designing such stages is to recover its stable flow range based on insights of compressor stability.

Compressor stability is a crucial issue on the reliability of gas turbine engines, and relating researches have lasted for almost a century. To date, mainly three groups of instabilities have been identified, namely surge, rotating stall, and rotating instability in descending order of time and length scale [3].

Surge is the breakdown of the compression system that results in large oscillations of flow properties propagating through the streamwise direction. Its length scale is at the order of the streamwise length of the compression system, and its time scale is at the order of the system Helmholtz frequency. According to the oscillation intensity and the occurrence of reverse flows, the surge phenomenon can be further classified into mild surge without reverse flows and deep surge with reverse flows [4]. Mild surge usually occurs at low mass flows before the emergence of the deep surge, but it can also exist in the middle of a constant speed line in some centrifugal compressor cases [5–8]. Deep surge always emerges beyond the lowest mass flow. It often leads to drastic fluctuations in pressure, flow rate and noise and even results in catastrophic failure of the whole system. In addition to the streamwise oscillation, the surge may also present non-axisymmetric flow patterns. The occurrence of the surge could be restricted to partial spans [9]. A phase lag may exist among surge signals at different circumferential locations [10,11]. This non-axisymmetric pattern could generate a radial force that eventually leads to severe blade rubbing.

The nature of surge was unveiled by the lumped parameter model of Greitzer [12]. It considered the filling and discharging process by a plenum model and the flow inertia by a duct model, along with the small perturbation theory for linearization. The model not only successfully reproduced similar fluctuations of flow parameters to experiments but differentiated the occurrence of the surge and rotating stall by the non-dimensional $B$ parameter. Following research aimed to improve the model accuracy by both experimental and numerical approaches: one-dimensional CFD simulations of the real piping systems

* Corresponding author.
*E-mail addresses:* hex15@mails.tsinghua.edu.cn (X. He), zhengxq@tsinghua.edu.cn (X. Zheng).

https://doi.org/10.1016/j.expthermflusci.2018.06.023
Received 16 February 2018; Received in revised form 26 May 2018; Accepted 23 June 2018
Available online 17 July 2018

**Nomenclature**

| | |
|---|---|
| $a$ | sound velocity [m/s] |
| $A$ | duct cross-sectional area [$m^2$] |
| $b$ | blade height [m] |
| $c_p$ | specific heat capacity at constant pressure [J/(kg K)] |
| $C$ | static pressure rise across the compressor [Pa] |
| $F$ | damper constant [kg/s] |
| $G$ | static pressure drop across the throttle [Pa] |
| $K$ | spring constant [N/m] |
| $L$ | duct length [m] |
| $m$ | mass flow rate [kg/s] |
| $M$ | mass [kg] |
| $r$ | distance in the radial direction [m] |
| $U$ | blade speed [m/s] |
| $V$ | volume of the plenum [$m^3$] |
| $Z$ | number of blades [–] |
| $\gamma$ | heat capacity ratio [–] |
| $\pi$ | pressure ratio [–] |
| $\rho$ | density [kg/$m^3$] |
| $\upsilon$ | kinematic viscosity [$m^2$/s] |
| $\omega_n$ | natural frequency [Hz] |
| $\zeta$ | damping ratio [–] |

*Abbreviations*

| | |
|---|---|
| BPF | blade passing frequency |
| IPF | impeller passing frequency |
| SP | stability parameter |

*Definition of non-dimensional parameters*

| | |
|---|---|
| $B$ | Greitzer's B parameter $\frac{U}{2a}\sqrt{\frac{V}{AL}}$ |
| $Mu$ | impeller tip Mach number $\frac{U_2}{\sqrt{\gamma R T_{t1}}}$ |
| $Re$ | Reynolds number $\frac{U_2 b_2}{\upsilon_1}$ |
| $\varphi$ | flow coefficient $\frac{m}{4\rho_{t1} U_2 r_2^2}$ |
| $\lambda$ | work coefficient $\frac{c_p T_{t1}\left(\pi^{\frac{\gamma-1}{\gamma}}-1\right)}{\eta U_2^2}$ |
| $N_s$ | specific speed $\frac{2\varphi^{1/2}}{\lambda^{3/4}}$ |

*Subscripts*

| | |
|---|---|
| *1* | impeller inlet (ambient) |
| *2* | impeller exit |
| *4* | diffuser exit |
| *6* | volute exit |
| *t* | total quantity |
| II | transducer location at impeller exit |
| III | transducer location at diffuser half section |
| IV | transducer location at diffuser exit |

were proposed to replace the duct and the plenum model [13]; special experimental procedures were designed to accurately measure the compressor pressure rise characteristic under unstable conditions [14].

Rotating stall is the circumferential propagation of single or multiple low-momentum cells (or stall cells) that limits the compressor pressure rise. Its length scale is at the order of the compressor circumference, and its time scale is on the order of impeller passing frequency (IPF). Emmons et al. [5] proposed a definite phenomenological model about the mechanism of rotating stall: when the first stall cell is formed in a blade passage, it blocks the incoming flow and causes an incidence spike on the adjacent blade, which drives the adjacent blade to stall, and thus the stall cell rotates.

Subsequent research of rotating stall focused on how the first stall cell was initiated. So far, the long-length-scale modal-type stall inception and the short-length-scale spike-type stall inception have been identified. The modal-type stall is triggered by a small full-span disturbance whose circumferential wavelength is equivalent to the annulus. It occurs near the zero slope of the compressor pressure rise characteristic, and the time from the stall inception to the fully-developed rotating stall is about tens of rotor revolutions. The long-length-scale perturbation that triggers rotating stall can be theoretically predicted. Because of its relatively low amplitude and growth rate, the perturbation can be restrained by active control methods before the rotating stall develops mature [15]. The spike-type stall is initiated by a spike-like disturbance near the blade tip whose circumferential wavelength is only two to three blade passages. It appears at a negative slope of the compressor pressure rise characteristic, and it develops from initial stage to mature stall cells within five rotor revolutions [16]. Recently, the mechanism of the spike-like disturbance has been determined as the formation of a radial vortex connecting the blade suction surface and the casing wall [17]. Although evidence in support of the mechanisms keeps accumulating in axial compressors [18–20], it is not necessarily the case in some centrifugal compressors: radial vortex structures were observed in both the impeller and the vaned diffuser, but the compressor presented modal-type stall instead of spike-type stall [21]. Thus, further experimental studies on cases of current interest are required.

Rotating instability is the pre-stall disturbance that is continually changing in amplitude and frequency. Its length scale is at the order of the compressor blade pitch, and its time scale at the order of blade passing frequency (BPF) [22]. Rotating instability usually exists in cases with large tip gaps, and its mechanism was proposed to be the circumferential movement of the radial vortex inside a blade passage [23]. Although certain similarity between the rotating instability and the spike disturbance that triggers rotating stall exists, they are not the same phenomenon as rotating instability emerges well before the stall onset and lasts for a long time. In our previous research, rotating instability was also observed in a centrifugal compressor and was referred to as high-frequency pressure oscillation [10] or high-frequency stall [24].

Among the brief review of multiple compressor unstable phenomena, fundamental understandings towards compressor stability have been achieved. However, most case studies were involved in axial compressors rather than centrifugal compressors, and differences between those two categories do exist. Because the centrifugal force provided by the impeller radial part counteracts against the streamwise adverse pressure gradient and stabilizes the whole impeller, the impeller axial part can operate under more severe unstable conditions than axial compressors do. For impellers with high inlet tip to outlet radius ratios, large areas of inlet recirculations occur when operating at low mass flows at part speeds, which leads to the impeller stall [25]. The inlet recirculation is different from the conventional rotating stall [26] but instead appears as the symmetrical blockage around all the annulus. Due to the streamline curvature and the Coriolis force in the impeller passage, the strength of its secondary flow is stronger than the axial compressor, resulting in a significant spanwise distortion of the vaned diffuser incoming flow [27]. As a consequence, the flow instability of vaned diffusers may occur at either the shroud section like the spike-type rotating stall [28] or at the hub section like the hub-suction surface corner stall [29]. Moreover, the compressor stability issue for high pressure ratio centrifugal compressors is expected to be more complex than ordinary centrifugal cases. The inlet condition of

the impeller tip and the vaned diffuser will become supersonic at high pressure ratio conditions. Therefore, shock waves and shock-boundary layer interactions will occur at the impeller tip and the vaned diffuser mid-span, which further deteriorate the flow stability by turning the boundary layer prone to flow separations. The matching conditions between the impeller and the vaned diffuser will vary drastically across speeds, especially when the design pressure ratio is high. The motivator of flow instabilities can switch from one component to another, resulting in complex flow instability mechanisms.

The motivation of this paper is to advance the understanding of the instability pathology of high pressure ratio centrifugal compressors. To start with, the experimental methodology and the investigated case is explained in detail. Then, steady performances of components and the entire stage are analyzed. Finally, transient pressure measurements are analyzed, and the evolution process from stable to unstable conditions at different speeds is discussed.

## 2. Methodology

### 2.1. Case description

The investigated high pressure ratio centrifugal compressor is an in-house prototype design, whose specifications are presented in Table 1. The impeller and the vaned diffuser were manufactured by flank milling of titanium alloy and stainless steel, respectively. The vaned diffuser disc was installed in the casing. A volute was attached downstream the vaned diffuser. Following the matching strategy of Casey and Rusch [30], the impeller and the vaned diffuser were matched to choke at the same time when operating at the design speed. The picture of the test compressor is presented in Fig. 1.

### 2.2. Experiment setup

The schematic diagram of the test rig is illustrated in Fig. 2. Pressurized air is heated by a combustor and then expands in the turbine to drive the compressor at a constant speed. A plenum is placed in front of the compressor where the inlet pressure and temperature are measured and kept constant. The mass flow rate is measured by the Venturi flowmeter after the plenum, which has an uncertainty of ± 2.36 $\times 10^{-3}$ $m^3/s$ near the choke condition. A performance tube with thermal insulation is attached to the compressor exit in which the total pressure and total temperature are measured. Pressure sensors have an uncertainty of ± 0.05% of the full-scale range, and resistance thermometers have an uncertainty of ± 0.6 K. The back pressure of the compressor is adjusted through the throttle downstream. The rotational speed is measured by a magnetoresistive sensor at the compressor inlet. The ambient pressure and temperature are also measured to correct the mass flow rate and the rotation speed. For each performance map, the test starts from choke to surge and from low speed to high speed. Data are recorded when the fluctuation of the compressor efficiency and the corrected rotational speed in one minute is within ± 0.1% and ± 200 RPM, respectively.

Previous research has proved the capability of pressure transducers to detect compressor flow instabilities across scales [32]. In this paper, fifteen piezoresistive fast response pressure transducers from Kulite were mounted into the casing, all of which has an uncertainty of ± 0.1% of the full-scale range. The XTE-140 (M) series pressure transducers were applied to the impeller inlet, while the XTEH-10L-190 (M) series pressure transducers are applied to downstream sections concerning their reliability under high temperature. Labels and locations of each transducer are illustrated in Fig. 3. The precise coordinates of each transducer are presented in Table 2. It should be noted that the measured pressure is a spatial-averaged value over the transducer measure plane. The measure plane diameter of the XTE-140 (M) series is about one-third of the impeller inlet passage pitch, and that of the XTEH-10L-190 (M) series is about a quarter of the vaned diffuser inlet passage pitch. Signals from transducers were transmitted to the high-speed synchronous acquisition equipment. The sampling frequency of each pressure channel was set to 200 kHz, which is over four times of the BPF at the maximum speed.

### 2.3. Experiment repetition test

Performance curves of the same compressor were tested two times in different days, as compared in Fig. 4. The difference of the pressure ratio is within 0.1, and that of the minimum mass flow of each constant speed line is within $3 \times 10^{-3}$ kg/s. Thus, the experimental method is reliable enough to produce repetitive test results.

## 3. Compressor performance

Compressor stability is characterized by its constant capability of delivering a higher pressure ratio when the mass flow rate decreases. To give an overview of the stability of high pressure ratio centrifugal compressors, the time-averaged performance of both the compressor stage and components are examined in this section.

### 3.1. Stage performance

The performance and stability map of the investigated compressor is shown in Fig. 5. Within the measured speed lines, operating conditions including deep surge, mild surge, stall, rotating instability and stable state are identified. The deep surge point marked by a cross was quickly determined by seeing a transient significant flow reduction from the flowmeter and hearing a powerful bump sound during the experiment. It should be noted that the mass flow rate and pressure ratio fluctuate violently during deep surge cycles. The coordinates of those points given in the figure are transient values obtained before the deep surge onset during the throttling process. The mild surge point presented by a diamond was determined by seeing a peak in frequency spectrums near the system Helmholtz frequency, as well as by hearing an audible bubble sound in the experiment. Since the mass flow rate and the pressure ratio of mild surge conditions slightly fluctuate with time, time-averaged values are shown in the figure. The stall point labeled by a square was defined near the peak pressure ratio conditions, where signals with frequencies between the Helmholtz frequency and the IPF are simultaneously profound. The stall signal was not circumferentially rotating, since there were neither peaks existed in frequency spectrums between 10–90% of the IPF, nor evident similarity found during the cross-correlation analysis between signals of impeller inlet transducers. The rotating instability point marked by a triangle was confirmed when a broadband hump between IPF and BPF was observed in frequency spectrums. Pressure signals and frequency spectrums will be detailed in Section 4.

Based on the stability condition of each operating point, the performance map can be divided into three sections. From 60% to 80%

**Table 1**
Specification of datum compressor TTL-1-Scale.

| Parameters | Symbols | Values |
|---|---|---|
| Number of impeller blades | $Z_I$ | 24 |
| Leading edge hub radius | $r_{1h}/r_2$ | 0.26 |
| Leading edge tip radius | $r_{1t}/r_2$ | 0.65 |
| Number of diffuser vanes | $Z_D$ | 19 |
| Diffuser leading edge radius | $r_3/r_2$ | 1.10 |
| Diffuser trailing edge radius | $r_4/r_2$ | 1.48 |
| Impeller tip Mach number | $Mu$ | 1.80 |
| Stage total pressure ratio | $\pi_{1t\text{-}6t}$ | 6.18 |
| Reynolds number | $Re$ | $1.34 \times 10^5$ |
| Flow coefficient | $\varphi$ | 0.06 |
| Work coefficient | $\lambda$ | 0.75 |
| Specific speed | $N_s$ | 0.61 |

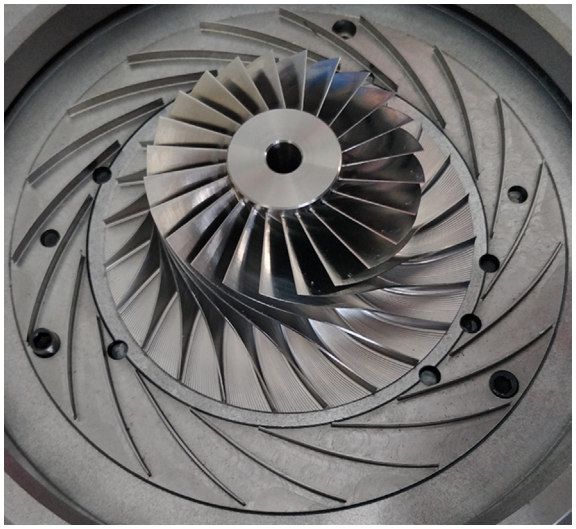

**Fig. 1.** TTL-1-Scale impeller reversely placed on its casing.

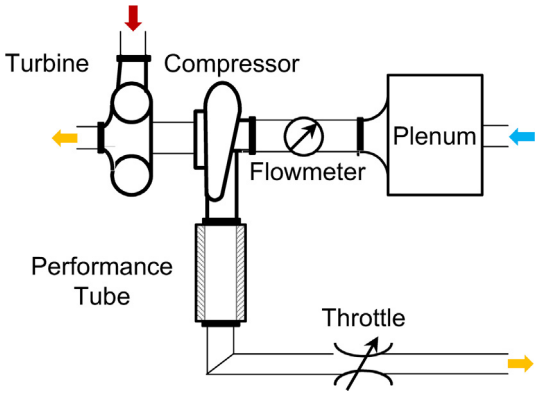


**Fig. 2.** Schematic diagram of the test rig.

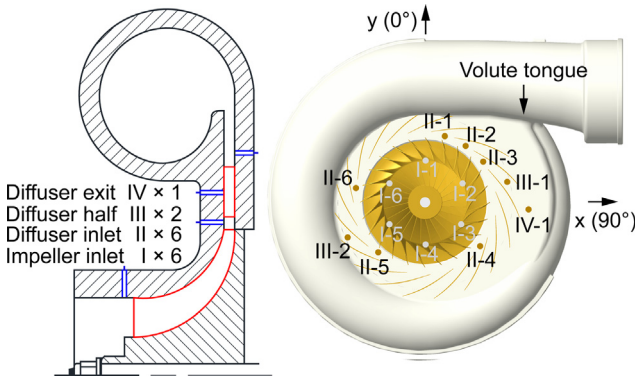


**Fig. 3.** Schematic of transducers setup.

**Table 2**
Location of the pressure transducers.

| Sections | $r/r_2$ | $\theta$ (deg) |
|---|---|---|
| I | 0.65 | 0, 60, 120, 180, 240, 300 |
| II | 1.10 | 15, 34, 53, 129, 224, 280 |
| III | 1.29 | 73, 244 |
| IV | 1.60 | 94 |
| Volute tongue | 1.76 | 54 |

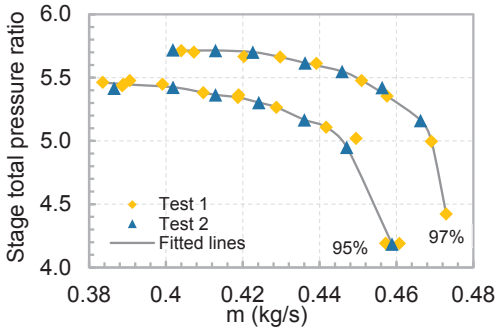


**Fig. 4.** Repetitive test results comparison.

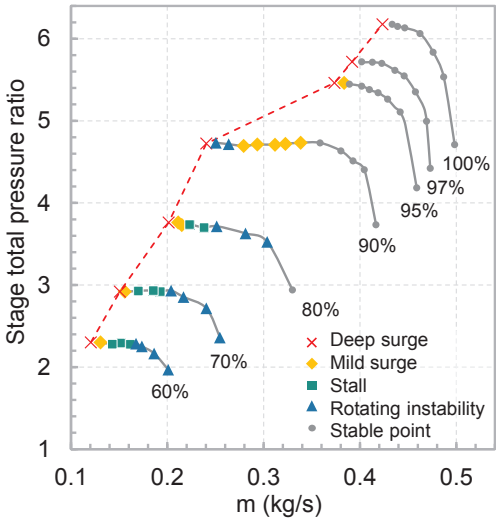


**Fig. 5.** Performance and stability map.

design speed, the compressor experiences rotating instability, stall, mild surge and deep surge when throttling the compressor. The 90% design speed is a dividing line where the two-regime-surge phenomenon occurs: when continuously reducing the mass flow rate, the compressor goes into mild surge first, then mild surge vanishes and rotating instability dominates, and deep surge occurs at last. The two-regime-surge behavior was previously reported in centrifugal compressors with vaneless diffusers [4,7,8]. It is the first time that the two-regime-surge is captured in a centrifugal compressor with a vaned diffuser. Compared to the vaneless diffuser cases, the two-regime-surge occurs at a much higher pressure ratio. The pressure rise characteristic of the 90% speed firstly decreases and then recovers with the reducing mass flow, which presents an S-shape. The mild surge occurs near its inflection point where the compressor pressure rise slope is locally maximum. From 95% to 100% design speed, the deep surge boundary suddenly moves to a much higher mass flow rate, and the compressor directly enters surge from stable conditions.

### 3.2. Component performance

For a compression system, a well-established criterion to identify the stability is the slope of its total-to-static pressure ratio characteristic. The flow is considered stable when the slope is not greater than zero [4]:

$$\frac{\partial(p_e/p_{ti})}{\partial m} \leqslant 0 \tag{1}$$

The stage total-to-static pressure ratio of the current case can be divided into the impeller part and the vaned diffuser part. Thus, the criterion in Eq. (1) becomes:

$$\frac{1}{\pi_{1t-IV}}\frac{\partial \pi_{1t-IV}}{\partial m} = \underbrace{\frac{1}{\pi_{1t-II}}\frac{\partial \pi_{1t-II}}{\partial m}}_{\text{Impeller}} + \underbrace{\frac{1}{\pi_{II-IV}}\frac{\partial \pi_{II-IV}}{\partial m}}_{\text{Vaned diffuser}} \leqslant 0 \quad (2)$$

A qualitative way to judge the stability of a component is to check whether its pressure rise characteristic has a positive or negative slope. The impeller and the vaned diffuser performance is shown in Fig. 6, where the pressure ratio is calculated using the time-averaged pressure from the compressor inlet and the transducers II-3 and IV-1. The impeller pressure curves from 60% to 90% design speed have almost zero slopes, indicating its strong instability under part speeds impeller-diffuser mismatching conditions. On the other hand, the vaned diffuser curves at equal speeds show negative slopes, which stabilizes the whole compressor stage. From 95% to 100% design speed, both the impeller and the vaned diffuser slope turns neutral near surge. It is hard to tell which component leads the system to surge.

A quantitative way to evaluate the contribution of each component to the stage stability is to calculate the value of each right-hand side term in Eq. (2), which is defined as the stability parameter (SP). The higher the SP value, the more unstable the component becomes. For calculating the pressure ratio of each component, the time-averaged pressure from the compressor inlet and the transducer II-3, III-1, and IV-1 are applied. A natural cubic spline is used to fit the pressure ratio characteristic, and the first order derivative of the pressure ratio can be computed from the spline formula.

The SP values of each component at 70%, 90%, and 100% design speed are plotted in Fig. 7. In general, the impeller and the vaned diffuser front part stay stable (negative SP value) at high mass flows, which is determined by the pressure rise characteristic of the compressor cascade. The vaned diffuser rear part is unstable (positive SP value) at almost all operating conditions because a lower mass flow leads to the enhanced blockage at the diffuser throat and thus the dropped pressure rise of the diffuser passage. When the mass flow reduces, it is the impeller and the vaned diffuser front part that quickly turns unstable and drives the whole compressor to stall and surge. This is due to the increased incidence and thus the developed blockage that hinders the pressure rise capability of the impeller and the vaned diffuser front part. The general findings of the component stability are in accordance with the previous research [31].

At 70% design speed, the impeller becomes unstable at first and initiates the stall, while the vaned diffuser stabilizes the compressor stage. When further reducing the mass flow, the vaned diffuser turns unstable as well, and mild surge and deep surge occur in the compressor. At 90% design speed, the impeller turns unstable first and then becomes stable, which generates a mild surge zone in the middle of the constant speed line. Meanwhile, the vaned diffuser maintains stable at mild surge conditions, indicating its irrelevance with the formation of the mild surge. When the mass flow decreases further, the vaned diffuser turns unstable, and the compressor enters deep surge. At 100% design speed, the vaned diffuser abruptly turns unstable while the impeller keeps stable, which directly results in the deep surge of the compressor.

## 4. Instability composition and evolution

Flow phenomena leading to compressor instability have various time scales and length scales. To detail the instability composition and the evolution from stable to unstable operating conditions, transient pressure signals inside the compressor are analyzed in both the time domain and the frequency domain in this section. Representative speeds including 70%, 90%, 95% and 100% design speed are investigated for low-speed, middle-speed and high-speed conditions, respectively. Considering the diffuser passage near the volute tongue is most prone to flow instabilities along the circumference [33], the following analysis focuses on transducers near the volute tongue, namely I-1, II-3, III-1, and IV-1.

### 4.1. Low-speeds: from rotating instability to stall

Frequency spectrums across the 70% design speed line are presented in Fig. 8, where the frequency is normalized by the IPF, the Fourier coefficient is normalized by the time-averaged pressure of the transducer, and the operating conditions with different mass flows are represented by different colors. At first glance, the IPF, the BPF, and their harmonics are quickly identified in all spectrums, whose frequency can be computed by the shaft speed and the blade number. Those signals directly related to the shaft rotation are natural references for distinguishing the scale of flow instabilities.

From 0.25 kg/s to 0.20 kg/s, a broadband hump between IPF and BPF is observed at the impeller inlet spectrum in Fig. 8(a), indicating the occurrence of rotating instability. Rotating instability is a well-documented flow phenomenon in previous axial compressor research. The nature of it is the circumferential movement of the inter-blade radial vortex. Because of the size and the speed of radial vortex fluctuate with time, a broadband hump in the frequency spectrum will be formed. The frequency at the hump peak is about 30% BPF in previous axial cases [3]. In the current case, this frequency ranges from 19% to 27% of BPF across the whole speed line, which is comparable to the axial one. When the incidence at the impeller inlet increases with the reduced the mass flow, the hump of rotating instability extends in breadth and moves to the low-frequency direction, indicating its development in scales.

From 0.19 kg/s to 0.17 kg/s, a second hump is induced below the IPF at spectrums of both the impeller inlet and the vaned diffuser inlet in Fig. 8. Its occurrence coincides with the peak pressure ratio condition of the impeller and the compressor stage. Thus, those signals are closely related with the impeller stall. Unlike the conventional rotating stall phenomenon of axial compressor rotors, the current stall signal shows a low-frequency hump in the spectrum rather than a discrete spike, revealing the stall signal has various scales of vortex structures. No evident circumferential propagation of the stall signal is found either in the cross-correlation analysis between transducers I-1 to I-6. The nature of the stall signal is supposed to be the impeller inlet flow recirculation, which is also called the inducer stall or the ring stall. The inlet flow recirculation originates from the leading edge flow separation under high incidence conditions. It is a form of the axisymmetric blockage around the circumference that contains vortex structures with diverse scales [26]. When the flow recirculation area extends to the downstream part of the impeller, it is likely to influence the vaned diffuser inlet through affecting the tip leakage flow. All of these features conform to the experimental observation. However, the deduction needs to

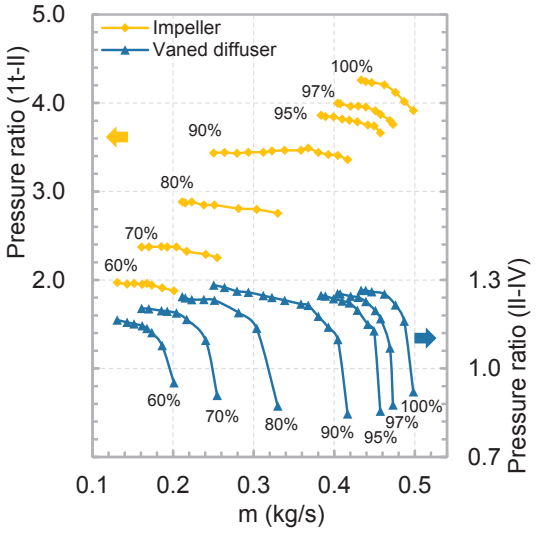


**Fig. 6.** Pressure rise characteristic of the impeller and the vaned diffuser.

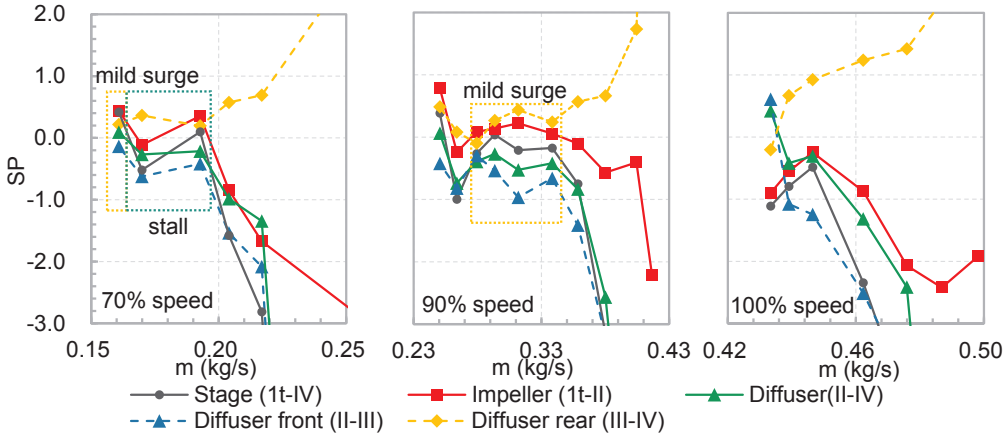


**Fig. 7.** Stability parameter values at 70%, 90%, and 100% design speed.

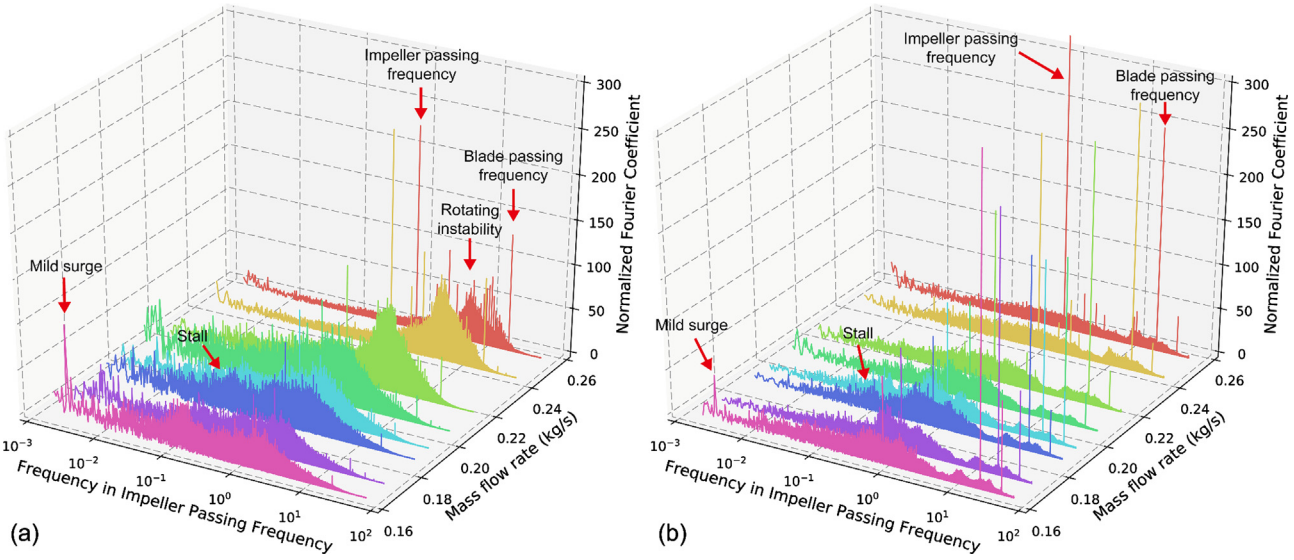


**Fig. 8.** Fast Fourier Transformation analysis at (a) impeller inlet (I-1) and (b) diffuser inlet (II-3), 70% design speed.

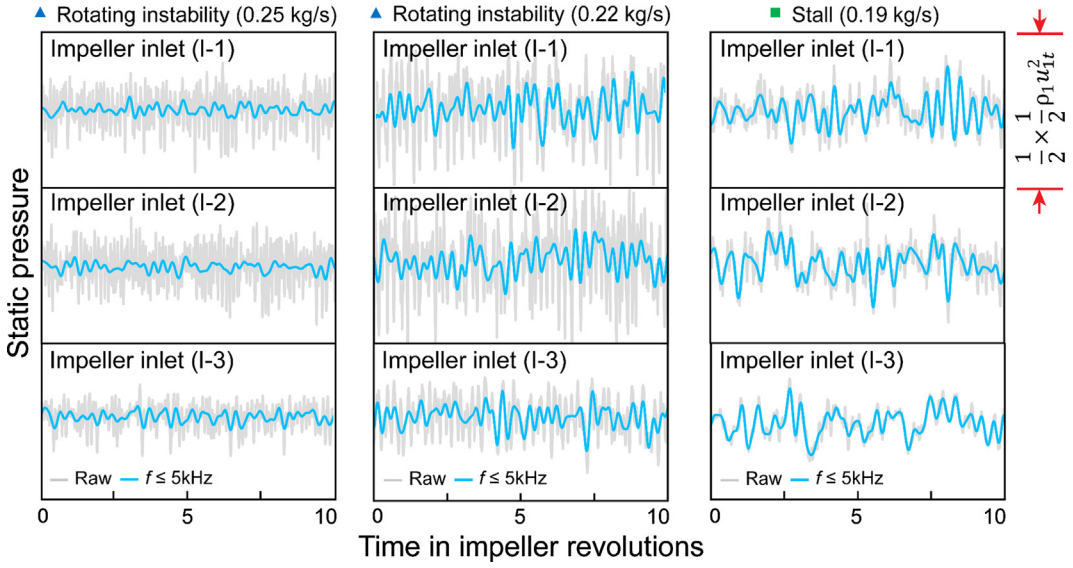


**Fig. 9.** Impeller inlet (I-1, I-2, and I-3) static pressure traces at rotating instability and stall conditions, 70% design speed.

be validated in future CFD simulations.

When further throttling the compressor to 0.16 kg/s, the slightly dropped compressor pressure curve triggers the mild surge of the compression system, which corresponds to the peak near the Helmholtz frequency at both the impeller and the diffuser inlet spectrums in Fig. 8. Deep surge eventually follows, and the compressor system breaks down.

To supplement the spectrum-based discussion, impeller inlet pressure traces of the raw signal and the low-pass filtered signal are depicted by grey curves and blue curves respectively in Fig. 9. The cutoff frequency of the low-pass filter is set at 5 kHz, which is about 3.5 times of IPF. The purpose of inducing the low-pass filtered signal is to present the waveform of the stall. Each subplot shares the same vertical axis scale, and subplots of the same mass flow are synchronized in time. At 0.25 kg/s, high frequency rotating instability signals dominate, and the amplitude of filtered traces are comparatively low. At 0.22 kg/s, wave structures of filtered traces present strong amplitudes, indicating the decrease of the rotating instability frequency. These wave structures are continuously changing in amplitude and wavelength without evident similarities found between different circumferential locations. At 0.19 kg/s, low-frequency stall waves dominate the full signal, because the low-pass filtered signal almost completely overlaps with the raw one. Again, the amplitude and the wavelength of the stall signal changes with time. Circumferential propagation of the pressure stall cell is not observed.

### 4.2. Middle-speeds: two-regime-surge

Frequency spectrums across the 90% design speed line are presented in Fig. 10, whose axes are in the similar fashion of Fig. 8. From 0.42 kg/s to 0.36 kg/s, only IPF, BPF, and their harmonics are observed in frequency spectrums at the impeller and the vaned diffuser inlets without any indication of instability. When the compressor stage reaches its peak pressure ratio at 0.34 kg/s, a discrete peak near the Helmholtz frequency appears in both frequency spectrums, which implies the occurrence of the mild surge. The mild surge signal develops and maximizes in amplitude at 0.31 kg/s where the maximum slope value of the compressor stage pressure ratio is also reached. Later, the mild surge signal vanishes and disappears at 0.28 kg/s, and a non-surge region is formed between 0.26 kg/s and 0.25 kg/s. Deep surge finally emerges and the compression system collapses. In the meantime, the rotating instability hump develops at the impeller inlet from 0.34 kg/s to 0.25 kg/s.

Static pressure traces at mild surge conditions are compared in Fig. 11, where the raw signal and low-pass filtered signals are depicted. The cutoff frequency of the low-pass filter is set at 5 kHz and 0.5 kHz, which is about 2.8 times and 28% of the IPF, respectively. Those low-pass filtered curves are applied to present the rotating instability and the mild surge. Subplots of the same transducer share the same vertical axis scale, and subplots of the same mass flow are synchronized in time. All the mild surge pressure waves present sinusoidal shapes and share similar periods across operating conditions and streamwise positions. An antiphase phenomenon is observed where wave crests of impeller inlet signals coincide with wave troughs of diffuser inlet signals, which is the consequence of the streamwise propagation of mild surge signals. When throttling the compressor, the mild surge signal firstly enhances and then diminishes in strength, as denoted by the amplitude of the orange curve. Meanwhile, the impeller inlet rotating instability signal develops in strength, as denoted by the amplitude of the blue curve. The coupling between rotating instability and the mild surge is also evident in Fig. 10(a).

The deep surge cycle is presented by static pressure traces at different streamwise locations in Fig. 12, where all pressure signals are synchronized and non-dimensionalized by the dynamic pressure. Based on the time that the pressure rapidly changes, the deep surge cycle can be roughly divided into a breakdown phase and a recovery phase.

Before the breakdown phase, the impeller inlet experiences a gradual increase in pressure, but no change in pressure is observed at other streamwise sections. When the breakdown phase initiates at 54.6 revolutions, the blockage at the impeller inlet suddenly increases, leading to the stagnation of incoming flow and thus an increase in impeller inlet pressure and a reduction in mass flow. The perturbation of the reduced mass flow propagates to the downstream compression system and triggers the flow reversal, which passes through the diffuser exit, the diffuser half section, and the diffuser inlet at 56.2, 56.7, and 57.5 revolutions in chronological order. The high-pressure reversed flow finally reaches the impeller inlet after the peak of the impeller inlet pressure at 61.6 revolutions.

During the breakdown phase, the pressure at all streamwise sections decreases with time because of the discharge process. A multi-step discharge process that resembles the Helmholtz resonance is observed in the vaned diffuser. When the pressure force that drives the reverse flow cannot overcome the compressor blade force, the flow direction will change again, leading to a sudden decrease in pressure at all streamwise sections. The pressure decrease ends first at the impeller diffuser at 430.8 revolutions, and then ends at the impeller inlet, the diffuser half section, and the diffuser exit at 434.4, 438.2, and 447.8 revolutions in chronological order. It indicates the end of flow reversal of the breakdown phase.

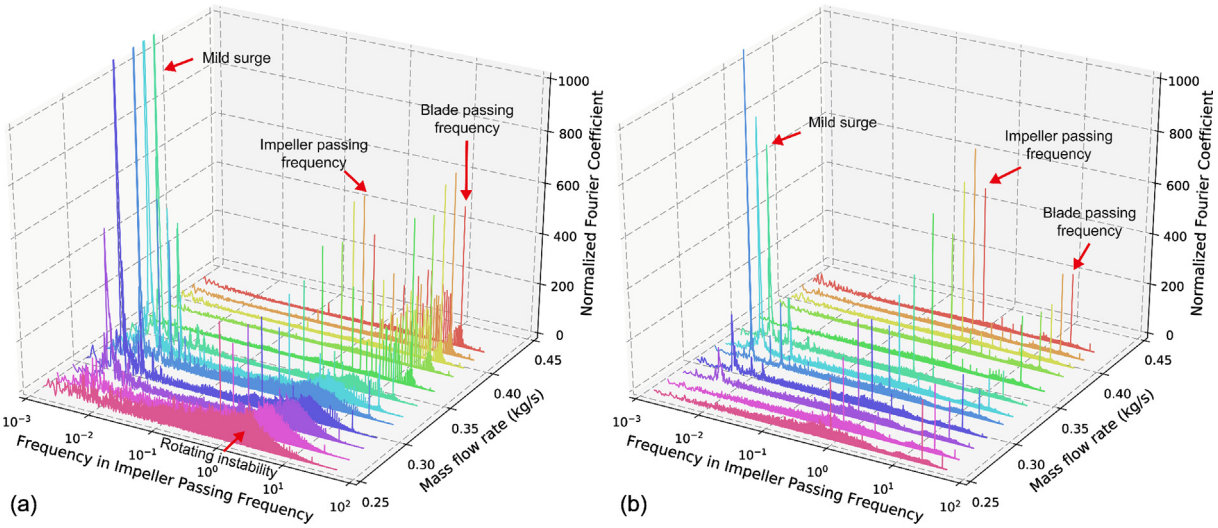


**Fig. 10.** Fast Fourier Transformation analysis at (a) impellerinlet (I-1) and (b) diffuser inlet (II-3), 90% design speed.

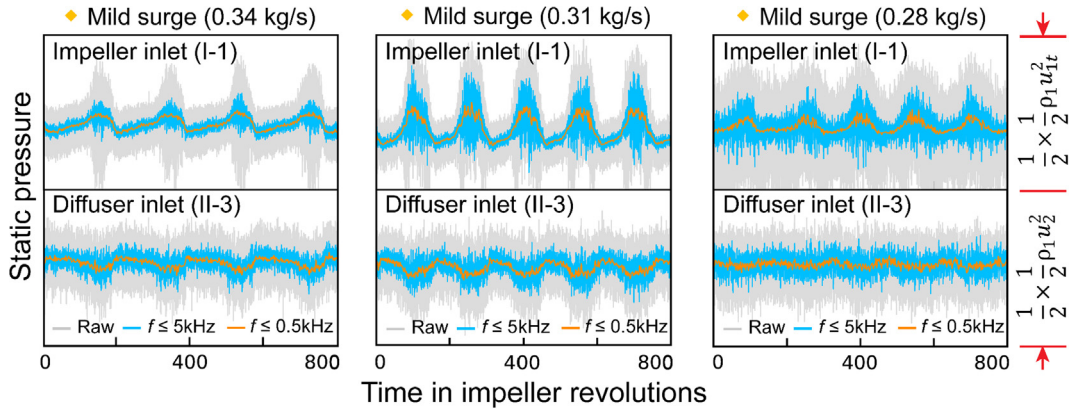


**Fig. 11.** Impeller inlet (I-1) and diffuser inlet (II-3) static pressure traces at mild surge conditions, 90% design speed.

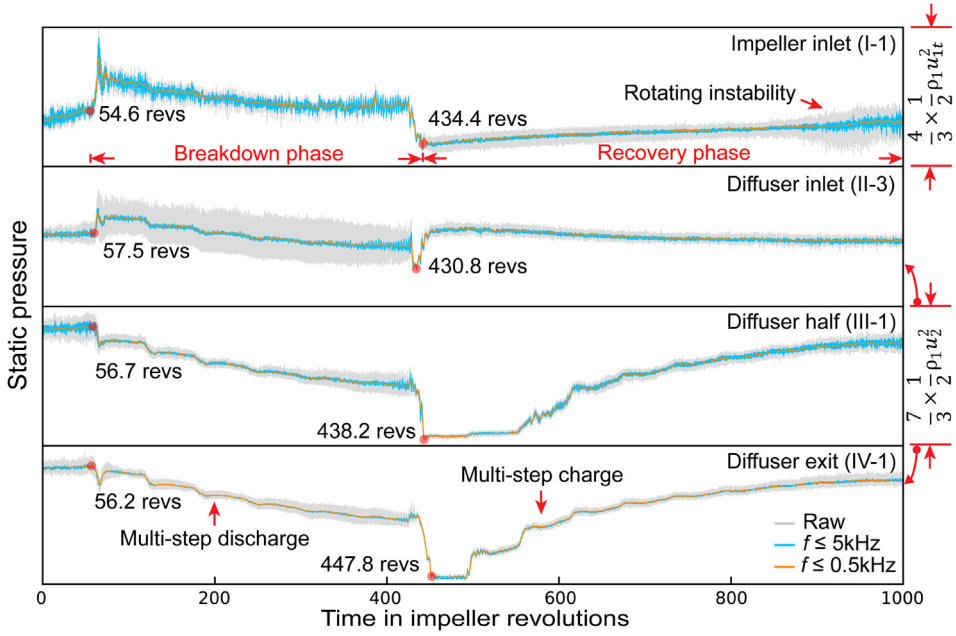


**Fig. 12.** Static pressure traces at deep surge conditions, 90% design speed.

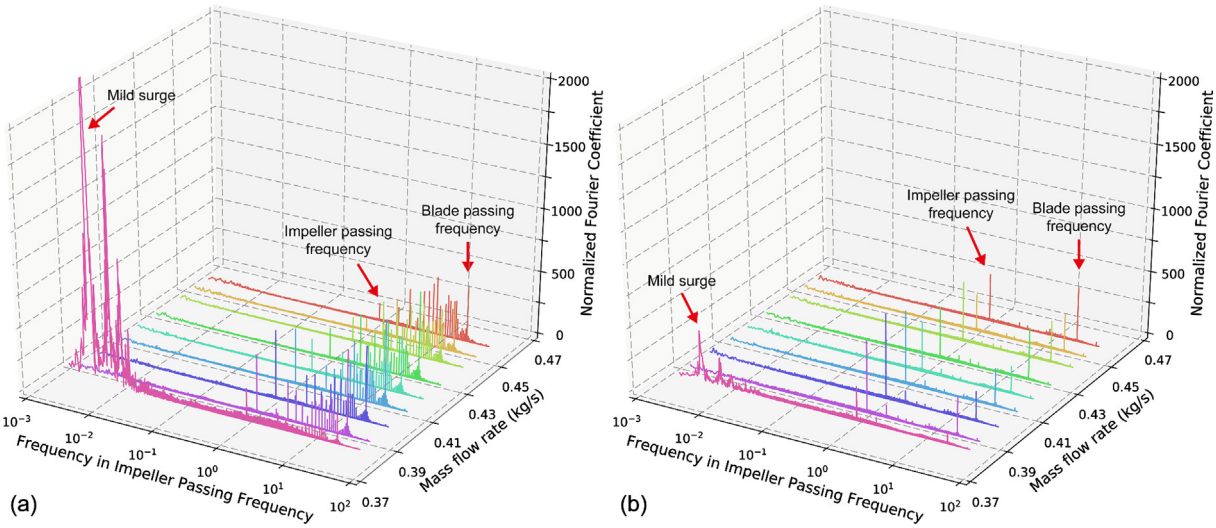


**Fig. 13.** Fast Fourier Transformation analysis at (a) impeller inlet (I-1) and (b) diffuserinlet (II-3), 95% design speed.

The recovery phase then begins where the pressure signal starts to recover to the state before the deep surge onset. A similar multi-step charge process that resembles the Helmholtz resonance is observed in the vaned diffuser. The rotating instability gradually develops at the impeller inlet, which is the reproduction of flow instabilities before the occurrence of the deep surge. After the end of the recovery phase and the beginning of the next breakdown phase, a complete deep surge cycle has been gone through.

### 4.3. High-speeds: abrupt occurrence of surge

Frequency spectrums across the 95% design speed line are presented in Fig. 13, whose axes are in the similar fashion of Fig. 8. Again, only IPF, BPF, and their harmonics are observed in frequency spectrums at the impeller and vaned diffuser inlets before the occurrence of the mild surge and deep surge. At even higher speeds or pressure ratios, the deep surge occurs without the prior presence of the long-lasting mild surge. The result indicates that component instabilities (i.e., rotating instability and stall) are not prerequisite of the surge, which is essentially a system behavior.

Surge cycles at high speeds are presented by static pressure traces in Fig. 14. At 95% design speed, a mild surge state exists before the deep surge. Comparing to mild surge cycles of middle speeds in Fig. 11, the gap between two adjacent peaks is much larger. When deep surge happens, several mild surge cycles are included in the recovery phase of the deep surge cycle. At 100% design speed, no long-lasting mild surge is captured before the onset of the deep surge.

## 5. Discussions on surge phenomenon

### 5.1. The stability model of the compression system

A simplified compression system is illustrated in Fig. 15(a), where the compressor is assumed quasi-steady, the duct is assumed to have all the inertia of the compression system without friction loss, and the variation of mass flow in the plenum is assumed to be isentropic. Considering a small perturbation $z$ of mass flow rate or compressor outlet pressure inputted in the system, the governing equation of the system can be deduced [4] as follows:

$$\frac{L}{A}\frac{d^2z}{dt^2} + \left[\frac{La^2}{AV}\left(\frac{dG}{dm}\right)^{-1} - \frac{dC}{dm}\right]\frac{dz}{dt} + \frac{a^2}{V}\left(1 - \frac{dC}{dm}/\frac{dG}{dm}\right)z = 0 \tag{3}$$

where $L$ and $A$ are the length and the cross-sectional area of the duct, $a$ and $V$ are the sound velocity and the volume of the plenum, and $G$ and $C$ are the pressure difference across the throttle and the compressor.

The governing equation of the compression system is in analogy to the mass-spring-damper system, which is illustrated in Fig. 15(b). Its governing equation writes as follows:

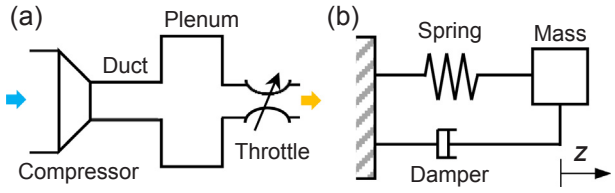


**Fig. 15.** Mechanical analogy: (a) simplified compression system; (b) mass-spring-damper system.

$$M\frac{d^2z}{dt^2} + F\frac{dz}{dt} + Kz = 0 \tag{4}$$

where $M$, $F$, and $K$ are the mass, the damper constant and the spring constant, respectively. The equivalent mass comes from the inertia in the duct. For the compression system, the equivalent damper constant originates from the characteristic of the throttle and the compressor. The throttle always leads to positive damping, but the compressor can bring either positive or negative damping determined by the operating point. The equivalent spring constant comes from the compressibility of the plenum fluid.

### 5.2. Mathematical mechanism of mild and deep surge

The surge mechanism of the compressions system can be better understood by studying the instability of the mass-spring-damper system. Such a system becomes unstable when either the spring constant or the damper constant becomes negative. The former is called the static instability, and the latter is the dynamic instability. When either constant equals zero, the corresponding compressor pressure rise slope is defined as the critical slope, which can be obtained as follows:

$$\left(\frac{dC}{dm}\right)_{stat} = \frac{dG}{dm} \tag{5}$$

$$\left(\frac{dC}{dm}\right)_{dyn} = \frac{La^2}{AV}\left(\frac{dG}{dm}\right)^{-1} \tag{6}$$

If the compressor pressure rise slope surpasses either critical values, the compression system will become unstable. Thus, the type of instability will be determined if its critical compressor slope is lower than its counterpart. To compare the value of both critical slopes, additional information about the test rig is needed. The duct length, the duct area, and the plenum volume are given in Table 3. The sound velocity of the plenum can be calculated by the local static temperature, which is approximated by the total temperature measured at the compressor exit. The throttle characteristic is assumed to be a parabola that passes through the origin of coordinate axes and the operating point of the compressor. Both critical slope values at the entire compressor range are compared in Fig. 16. It is found that the critical slope of the dynamic

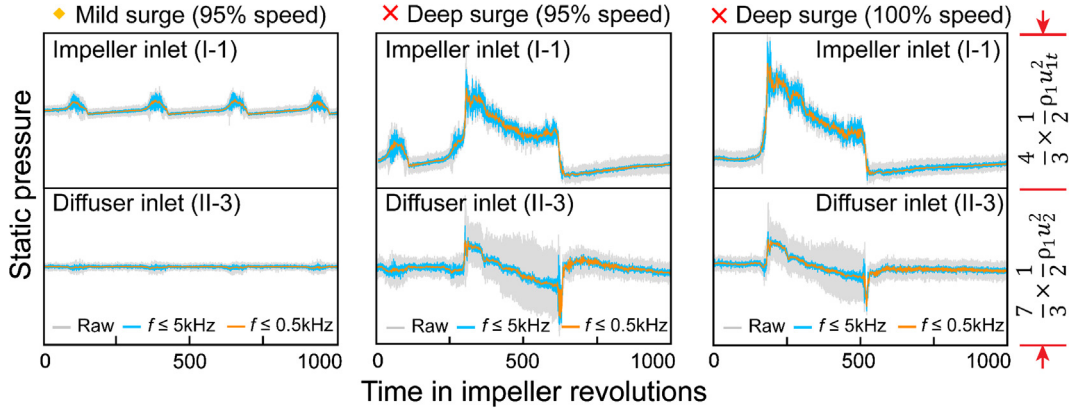


**Fig. 14.** Impeller inlet (I-1) and diffuser inlet (II-3) static pressure traces at mild surge and deep surge conditions, 95% and 100% design speed.

**Table 3**
Specification of the compression system.

| Component | Length (m) | Area ($m^2$) | Volume ($m^3$) |
|---|---|---|---|
| Perf. tube | 1.2 | $7.85 \times 10^{-3}$ | $9.42 \times 10^{-3}$ |
| Exit duct | 6.0 | $7.85 \times 10^{-3}$ | $4.71 \times 10^{-2}$ |
| Total | 7.2 | – | $5.65 \times 10^{-2}$ |

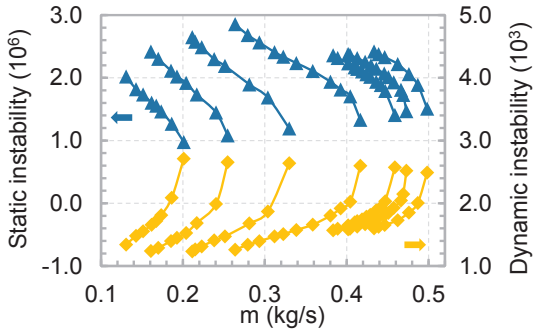


**Fig. 16.** Comparison of critical compressor pressure rise slope values.

instability is always of three orders lower than the static instability, indicating only the dynamic instability exists in the current compressor case.

Considering the system dynamic instability happens (M > 0, F < 0, K > 0), the solution form of Eq. (4) will determine the type of surge that occurs in the compression system. Using the natural frequency of the harmonic oscillator $\omega_n = \sqrt{K/M}$ and the damping ratio $\zeta = F/\sqrt{4MK}$, Eq. (4) is simplified as follows:

$$\frac{d^2z}{dt^2} + 2\zeta\omega_n\frac{dz}{dt} + {\omega_n}^2 z = 0 \tag{7}$$

The general solution of Eq. (7) is:

$$z = z_i e^{\lambda_i t} \tag{8}$$

where $\lambda_i$ is the eigenvalue of Eq. (7), calculated by the following equation:

$$\lambda^2 + 2\zeta\omega_n\lambda + {\omega_n}^2 = 0 \tag{9}$$

When the damping ratio $\zeta$ is greater than $-1$ but smaller than 0 (underdamped), the eigenvalues have non-zero imaginary parts. This scenario corresponds to an oscillation solution that resembles mild surge waves. When the damping ratio $\zeta$ is smaller than $-1$ (overdamped), the eigenvalues are two real numbers with opposite signs. In this case, the solution blows up exponentially similar to the deep surge onset. The aforementioned transient processes are illustrated in Fig. 17. Mathematically, mild surge and deep surge are two forms of solutions of a second order differential equation.

### 5.3. Physical mechanism of mild and deep surge

The physical mechanism of mild surge can be unveiled by checking the physical relevance of its oscillation frequency. According to the general solution in Eq. (8), the oscillation frequency of the mild surge is calculated as follows:

$$f = \frac{\omega_n}{2\pi}\sqrt{1-\zeta^2} \tag{10}$$

Replacing the natural frequency $\omega_n = \sqrt{K/M}$ by the equivalent constants shown in Eq. (3), the frequency is written as follows:

$$f = \frac{a}{2\pi}\sqrt{\frac{A}{LV}}\sqrt{1-\frac{dC}{dm}/\frac{dG}{dm}}\sqrt{1-\zeta^2} \tag{11}$$

Considering the onset of dynamic instability ($\zeta = 0$), the ratio of $dC/dm$ over $dG/dm$ equals to the ratio of $(dC/dm)_{dyn}$ over $(dC/dm)_{stat}$, which is three-order less than unity according to Fig. 16. Therefore, the oscillation frequency is reduced to the Helmholtz frequency of the compression system:

$$f \approx \frac{a}{2\pi}\sqrt{\frac{A}{LV}} \equiv f_{Helm} \tag{12}$$

By plugging in the experimental data of the first-appeared mild surge point at 0.34 kg/s and 90% speed, the Helmholtz frequency of the compression system is calculated to be 10.3 Hz, which is validated by the measured mild surge frequency of 9.5 Hz. Thus, the physics of mild surge is confirmed to be the Helmholtz resonance of the duct and the plenum of the compression system.

The physical process of a deep surge cycle is the discharge and recharge of the plenum flow, as discussed in Fig. 12. Its mechanism can be better understood by examing the physical relevance of the damping ratio, which decides the occurrence of the deep surge. By plugging the equivalent constants of Eq. (3) in the damping ratio $\zeta = F/\sqrt{4MK}$, the damping ratio $\zeta$ is written as follows:

$$\zeta = \left[\frac{La^2}{AV}\left(\frac{dG}{dm}\right)^{-1} - \frac{dC}{dm}\right]\cdot\left[\frac{4La^2}{AV}\left(1-\frac{dC}{dm}/\frac{dG}{dm}\right)^{-1}\right]^{-1/2} \tag{13}$$

The pressure difference and the mass flow can be non-dimensionalized using $\rho U^2/2$ and $\rho AU$ respectively. Eq. (13) therefore turns into the following form:

$$\begin{aligned}\zeta &= \frac{1}{2}\left(1-\frac{d\tilde{C}}{d\varphi}/\frac{d\tilde{G}}{d\varphi}\right)^{-1/2}\cdot\left[\frac{1}{B}\left(\frac{d\tilde{G}}{d\varphi}\right)^{-1} - B\frac{d\tilde{C}}{d\varphi}\right] \\ &\approx \frac{1}{2}\left[\frac{1}{B}\left(\frac{d\tilde{G}}{d\varphi}\right)^{-1} - B\frac{d\tilde{C}}{d\varphi}\right]\end{aligned} \tag{14}$$

where $\varphi$ is the flow coefficient, and the non-dimensional parameter $B$ is defined as follows:

$$B = \frac{U}{2a}\sqrt{\frac{V}{AL}} \tag{15}$$

The parameter $B$ is firstly derived by Greitzer [12]. It can be viewed as the compressor pressure rise capability over the required pressure rise to cause mass flow oscillations. According to Eq. (14), a high value of the parameter $B$ amplifies the positive slope of the compressor pressure rise characteristic, and the compressor system is thus more likely to have the deep surge occur rather than the mild surge. In the current case, the 95% design speed with a near-surge $B$ value of 0.63 is the critical condition. For operating speeds higher than 95% design speed, their $B$ values are higher than the 95% speed one, and the compression system directly enters into deep surge without observing evident mild surge states in advance. On the contrary, mild surge states can be easily captured before the occurrence of deep surge at lower operating speeds.

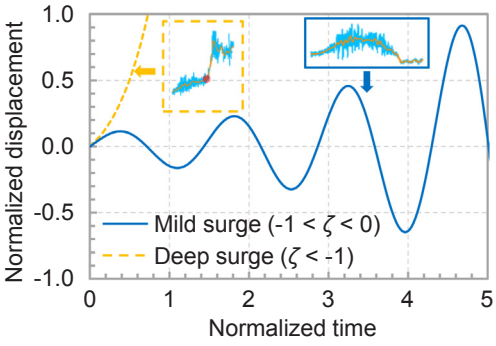


**Fig. 17.** Effects of damper constant on the dynamic instability transient.

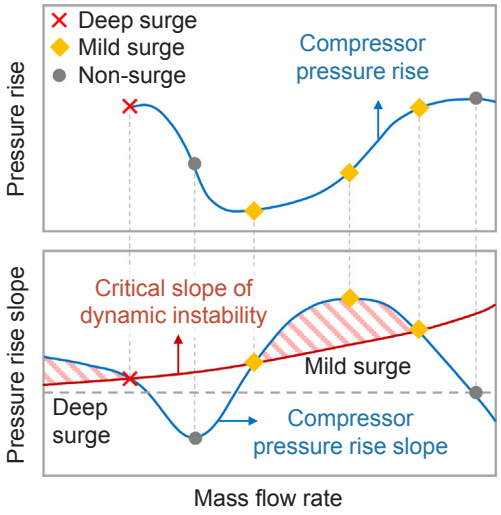


**Fig. 18.** Mechanism of the formation of two-regime-surge.

### 5.4. Mechanism of the two-regime-surge

On the 90% design speed, an interesting two-regime surge phenomenon along with the S-shaped compressor pressure rise characteristic is observed. A conceptual figure explaining the formation of the two-regime-surge is illustrated in Fig. 18. Given an S-shaped compressor pressure rise characteristic, its pressure rise slope will have two humps that intersect with the critical slope of dynamic instability three times, creating a mild surge zone at medium mass flows and a deep surge zone at low mass flows. Inside the mild surge region, the amplitude of the mild surge oscillation is correlated with the difference between the critical slope of the dynamic instability and the compressor pressure rise slope. Thus, the mild surge amplitude peaks near the maximum-slope point and vanishes near both ends of the mild surge zone, as observed in Fig. 10.

The S-shaped compressor pressure rise characteristic is the prerequisite of the above explanation. Such a feature is not only captured in the current case but also in previous studies [5–8] where the two-regime-surge were reported. The next question of interest is: why would a centrifugal compressor stage present an S-shaped pressure rise?

For the impeller side, the inlet flow recirculation will lead to a dip in the impeller pressure rise characteristic [25], which possibly forms the S-shape characteristic of the compressor stage. This scenario is demonstrated in a turbocharger centrifugal compressor [6]. In the current case, although Figs. 6 and 7 have implied the origin of the S-shape is the impeller, no inlet flow recirculation signals (similar to the stall signal observed at 60–80% speeds of the current case) were captured by transducers before the onset of the mild surge. The exact cause of the S-shape impeller characteristic of the current case needs to be checked in future CFD simulations.

For the vaned diffuser side, the vaned diffuser stall will cause a drop in the vaned diffuser pressure rise characteristic, which is also plausible to bring an S-shape characteristic of the compressor stage. A recent study reported the alternate stall phenomena in the vaned diffuser of an aeronautical centrifugal compressor stage with the S-shape characteristic, which is thought to lower down the pressure rise and trigger the mild surge in middle mass flows [11].

The mechanism of the S-shape pressure rise characteristic of the centrifugal compressor stage is still an open topic. More evidence is needed for future research.

## 6. Conclusions

The paper depicts a comprehensive map of instability evolution in a high pressure ratio centrifugal compressor with a vaned diffuser. Fast response pressure transducers were installed to unveil the compressor unstable phenomena with various time scales and length scales. Several conclusions are drawn as follows.

1. Diverse instabilities exist in the high pressure ratio centrifugal compressor, including mild and deep surge, inducer stall, and rotating instability in descending order of time and length scale.
2. At low speeds, the impeller inlet rotating instability develops in size and evolves into inducer stall, eventually leading to the mild surge and deep surge of the entire compression system. The surge of the compression system is induced by the impeller due to the mismatching between the impeller and the vaned diffuser at part speeds.
3. At middle speeds, the compressor successively experiences stable state, mild surge, rotating instability and eventually deep surge. Because of the S-shaped pressure rise characteristic of the impeller and the compressor stage, the compression system approaches the unstable underdamped state first and then recovers to the non-surge rotating instability state. Thus, mild surge with a sinusoidal wave shape and a natural frequency of the harmonic oscillator ephemerally occur. When further throttling the compressor, the motivator of surge switches from the impeller to the vaned diffuser and the compressor enters the deep surge state.
4. At high speeds, mild surge and deep surge abruptly emerge without preceding stall or rotating instability at either the impeller or the vaned diffuser. When the $B$ parameter of the compression system surpasses a critical value, which in this case is 0.63, the compression system directly enters deep surge without observing a long-lasting mild surge state. The surge of the compression system is caused by the vaned diffuser.

## Acknowledgement

This research was supported by the National Natural Science Foundation of China (Grant No. 51176087). The authors would like to thank Wuxi Itma Turbo Technologies for the assistance of experiments. Special thanks to Ms. Wenchao Zhang, Mr. Zitian Niu, Mr. Aolin Wang and Mr. Wangzhi Zou from Tsinghua Turbomachinery Laboratory for their effort in preparing the experiment and data post-processing.

## References

[1] H. Krain, Review of centrifugal compressor's application and development, J. Turbomach. 127 (1) (2005) 25–34.
[2] D. Japikse, Centrifugal Compressor Design and Performance, Concepts ETI Inc, Wilder, VT, 1996.
[3] I.J. Day, Stall, surge, and 75 years of research, J. Turbomach. 138 (1) (2016) 011001.
[4] N. Cumpsty, Compressor Aerodynamics, Kreiger Publishing Company, Malabar, FL, 2004.
[5] H. Emmons, C. Pearson, H. Grant, Compressor surge and stall propagation, American Society of Mechanical Engineers Paper 53-A-65, 1955.
[6] H. Tamaki, Study on flow fields in high specific speed centrifugal compressor with unpinched vaneless diffuser, J. Mech. Sci. Technol. 27 (6) (2013) 1627–1633.
[7] N. Diez, J. Smeulers, L. Tapinassi, et al., Predictability of rotating stall and surge in a centrifugal compressor stage with dynamic simulations, American Society of Mechanical Engineers Paper GT2014-26712, 2014.
[8] X. Zheng, A. Liu, Phenomenon and mechanism of two-regime-surge in a centrifugal compressor, J. Turbomach. 137 (8) (2015) 081007.
[9] T. Pan, Q. Li, Z. Li, Y. Gong, Effects of radial loading distribution on partial-surge-initiated instability in a transonic axial flow compressor, J. Turbomach. 139 (10) (2017) 101010.
[10] X. Zheng, Z. Sun, T. Kawakubo, H. Tamaki, Experimental investigation of surge and stall in a turbocharger centrifugal compressor with a vaned diffuser, Exp. Therm Fluid Sci. 82 (2017) 493–506.
[11] V. Moënne-Loccoz, I. Trébinjac, E. Benichou, S. Goguey, B. Paoletti, P. Laucher, An experimental description of the flow in a centrifugal compressor from alternate stall to surge, J. Therm. Sci. 26 (4) (2017) 289–296.
[12] E.M. Greitzer, Surge and rotating stall in axial flow compressors—Part I: Theoretical compression system model, J. Eng. Power 98 (2) (1976) 190–198.
[13] J. Galindo, J.R. Serrano, H. Climent, A. Tiseira, Experiments and modelling of surge

in small centrifugal compressor for automotive engines, Exp. Therm Fluid Sci. 32 (3) (2008) 818–826.
[14] S. Marelli, C. Carraro, G. Marmorato, G. Zamboni, M. Capobianco, Experimental analysis on the performance of a turbocharger compressor in the unstable operating region and close to the surge limit, Exp. Therm Fluid Sci. 53 (2014) 154–160.
[15] J.D. Paduano, E.M. Greitzer, A.H. Epstein, Compression system stability and active control, Annu. Rev. Fluid Mech. 33 (1) (2001) 491–517.
[16] C.S. Tan, I. Day, S. Morris, A. Wadia, Spike-type compressor stall inception, detection, and control, Annu. Rev. Fluid Mech. 42 (2010) 275–300.
[17] G. Pullan, A.M. Young, I.J. Day, E.M. Greitzer, Z.S. Spakovszky, Origins and structure of spike-type rotating stall, J. Turbomach. 137 (5) (2015) 051007.
[18] J. Dodds, M. Vahdati, Rotating stall observations in a high speed compressor—Part I: Experimental study, J. Turbomach. 137 (5) (2015) 051002.
[19] J. Dodds, M. Vahdati, Rotating stall observations in a high speed compressor—Part II: Numerical study, J. Turbomach. 137 (5) (2015) 051003.
[20] C. Brandstetter, H. Schiffer, PIV measurements of the transient flow structure in the tip region of a transonic compressor near stability limit, J. Global Power Propul. Soc. 2 (2018) 303–316.
[21] Y. Bousquet, N. Binder, G. Dufour, X. Carbonneau, M. Roumeas, I. Trebinjac, Numerical simulation of stall inception mechanisms in a centrifugal compressor with vaned diffuser, J. Turbomach. 138 (12) (2016) 121005.
[22] R. Mailach, I. Lehmann, K. Vogeler, Rotating instabilities in an axial compressor originating from the fluctuating blade tip vortex, J. Turbomach. 123 (3) (2001) 453–460.
[23] J. Marz, C. Hah, W. Neise, An experimental and numerical investigation into the mechanisms of rotating instability, J. Turbomach. 124 (3) (2002) 367–374.
[24] X. Zheng, A. Liu, Experimental investigation of surge and stall in a high-speed centrifugal compressor, J. Propul. Power 31 (3) (2015) 815–825.
[25] P. Harley, S. Spence, D. Filsinger, M. Dietrich, J. Early, Meanline modeling of inlet recirculation in automotive turbocharger centrifugal compressors, J. Turbomach. 137 (1) (2015) 011007.
[26] H. Tamaki, M. Unno, R. Tanaka, S. Yamaguchi, Y. Ishizu, Enhancement of centrifugal compressor operating range by control of inlet recirculation with inlet fins, J. Turbomach. 138 (10) (2016) 101010.
[27] J.N. Everitt, Z.S. Spakovszky, D. Rusch, J. Schiffmann, The role of impeller outflow conditions on the performance of vaned diffusers, J. Turbomach. 139 (4) (2017) 041004.
[28] J.N. Everitt, Z.S. Spakovszky, An investigation of stall inception in centrifugal compressor vaned diffuser, J. Turbomach. 135 (1) (2013) 011025.
[29] A. Marsan, I. Trébinjac, S. Coste, G. Leroy, Influence of unsteadiness on the control of a hub-corner separation within a radial vaned diffuser, J. Turbomach. 137 (2) (2015) 021008.
[30] M. Casey, D. Rusch, The matching of a vaned diffuser with a radial compressor impeller and its effect on the stage performance, J. Turbomach. 136 (12) (2014) 121004.
[31] R. Hunziker, G. Gyarmathy, The operational stability of a centrifugal compressor and its dependence on the characteristics of the subcomponents, J. Turbomach. 116 (2) (1994) 250–259.
[32] A. Liu, X. Zheng, Methods of surge point judgment for compressor experiments, Exp. Therm Fluid Sci. 51 (2013) 204–213.
[33] X. Zheng, Z. Sun, T. Kawakubo, H. Tamaki, Stability improvement of a turbocharger centrifugal compressor by a nonaxisymmetric vaned diffuser, J. Turbomach. 140 (4) (2018) 041007.